

Quantum Confinement and Electronic Properties of Rutile TiO₂ Nanowires

Haowei Peng and Jingbo Li*

State Key Laboratory for Superlattices and Microstructures, Institute of Semiconductors, Chinese Academy of Sciences, P.O. Box 912, Beijing 100083, People's Republic of China

Received: August 20, 2008; Revised Manuscript Received: October 23, 2008

The quantum confinement effect, electronic properties, and optical properties of TiO₂ nanowires in rutile structure are investigated via first-principles calculations. We calculate the size- and shape-dependent band gap of the nanowires and fit the results with the function $E_g = E_g^{\text{bulk}} + \beta/d^\alpha$. We find that the quantum confinement effect becomes significant for $d < 25$ Å, and a notable anisotropy exists that arises from the anisotropy of the effective masses. We also evaluate the imaginary part of the frequency-dependent dielectric function [$\epsilon_2(\omega)$] within the electric-dipole approximation, for both the polarization parallel [$\epsilon_2^{\parallel}(\omega)$] and the perpendicular [$\epsilon_2^{\perp}(\omega)$] to the axial (c) direction. The band structure of the nanowires is calculated, with which the fine structure of $\epsilon_2^{\parallel}(\omega)$ has been analyzed.

Nanosized semiconductor materials exhibit a pronounced quantum confinement effect on electronic structure. Their small size raises the conduction band and lowers the valence band. The resulting band shift affects related optical properties, such as optical absorption and photocatalytic properties of the semiconductors. TiO₂ is a wide band gap semiconductor used in both energy and environmental applications,¹ such as photocatalyst, self-cleaning material, and electrode in dye-sensitized solar cells (DSSCs). TiO₂ nanomaterials demonstrate particularly high performance levels for these applications because of their increased surface area. For example, the TiO₂ nanoparticle films have been used in DSSCs, resulting in a full sun efficiency of 10%.² However, there is a bottleneck of the power conversion efficiency arising from a hopping mechanism of charge transport between neighboring particles. Recently, the application of TiO₂ nanowires as photoactive materials and electrodes in DSSC has attracted much attention,^{3–6} for the band transport instead of the hopping transport mechanism can improve the external quantum efficiency of the devices. Besides, the improvements of techniques to synthesize the TiO₂ nanowires make the investigation feasible and easy.¹

The photophysical properties of TiO₂ nanoparticles displaying the quantum confinement effect have been investigated experimentally.^{7–9} We also have investigated this effect in rutile TiO₂ nanodots¹⁰ using the first-principles band-structure method. The band gap shift, ΔE_g , due to the quantum confinement effect in the TiO₂ nanodots, evolves as $73.70/d^{1.93}$, when the size of the nanodots, d , decreases. Our result agrees with the experiments⁷ very well. To our knowledge there are neither experiments nor theoretical studies on the quantum confinement effect in the TiO₂ nanowires. In this article, this fundamental property of the TiO₂ nanowires is studied and compared to the quantum confinement effects in the nanodots. An overly simplified particle-in-a-box effective-mass model gives a result of $\Delta E_g^{\text{wire}}/\Delta E_g^{\text{dot}} = 0.586$.¹¹ It is interesting to compare it to the result of our first-principles calculations. In addition, the shape-dependence of the quantum confinement effect, that is, whether the quantum confinement effect is anisotropic, is investigated too. Finally, to explore the effects of the quantum confinement on

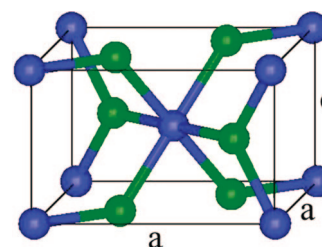


Figure 1. Primitive unit cell for TiO₂ in the rutile structure: the blue and green spheres represent the Ti and O atoms, respectively.

the optical properties, we present and analyze at length the imaginary part of the frequency-dependent dielectric functions for the nanowires.

In this study, the first-principles band-structure calculations are performed with the local density approximation (LDA) based on the density functional theory (DFT), as implemented in the Vienna ab initio simulation package (VASP).¹² The projected augmented wave (PAW) method¹³ is chosen to represent the ionic potentials. The Monkhorst–Pack method¹⁴ is used to sample the Brillouin zone. For all of the nanowires, a $1 \times 1 \times 16$ k -grid is used, while for the primitive cell of the bulk, a $12 \times 12 \times 16$ grid is used. For all calculations, the energy cutoff for the plane waves is 500 eV. The convergence with respect to the plane wave basis cutoff energy and the k -sampling is checked to be within 0.001 eV. Before the electronic structure properties were studied, the atomic configurations for all structures have been relaxed until the Hellmann–Feynman force is less than 0.01 eV/Å.

The primitive cell of TiO₂ in the rutile structure is shown in Figure 1. The space group of the tetragonal rutile structure is $P4_2/mnm$ (D_{4h}^{14}). The structure is defined by three crystallographic parameters: two lattice parameters, a , c , and the internal parameter, u . In the primitive cell, two Ti atoms are located at $(0, 0, 0)$ and $(1/2, 1/2, 1/2)$, and four O atoms at $\pm(u, u, 0)$ and $\pm(1/2 + u, 1/2 - u, 1/2)$. The three structure parameters are optimized using the Murnaghan's equation of state based on the LDA calculations, as compared to the experimental values in Table 1. These parameters are used to build the nanowires.

In this study, we have considered four kinds of nanowires to investigate the shape dependence of the quantum confinement

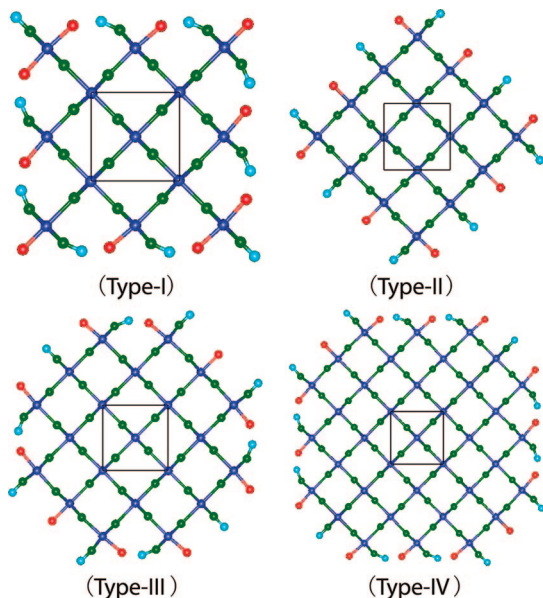
* Corresponding author. E-mail: jbli@semi.ac.cn.

TABLE 1: Calculated Structural Parameters of Rutile TiO₂, As Compared to the Experimental¹⁵ Results

| | this work | experiment |
|--------------|-----------|------------|
| <i>a</i> (Å) | 4.568 | 4.5936 |
| <i>c</i> (Å) | 2.926 | 2.9587 |
| <i>cla</i> | 0.641 | 0.6441 |
| <i>u</i> | 0.305 | 0.3048 |

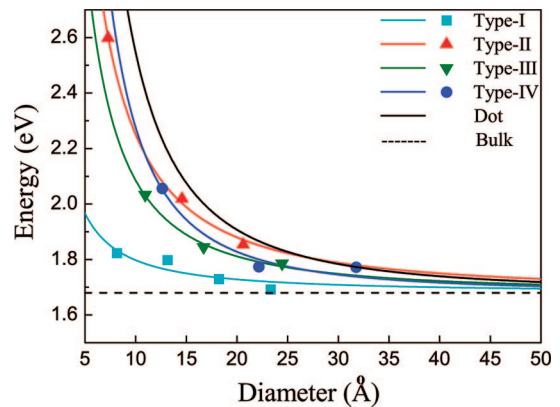
effect. All of the nanowires are periodically extended along the *c* axis. However, the shapes of their cross sections are different, as illustrated in Figure 2. For type-I nanowires, the (100) crystal faces of the rutile structure constitute the surfaces of the wires, (110) for type-II and type-III nanowires, and both of them for type-IV nanowires. The structural difference between the type-II and type-III nanowires is that the center of the type-II nanowires is a Ti atom, whereas the center of the type-III nanowires is a Ti–Ti pair along the [100] crystal direction. Yet for the type-IV nanowires, we will not consider this detail because their unit cells are so large that the size effect is more significant than the shape effect. The surface dangling bonds are terminated with pseudohydrogen atoms,^{10,11} which have fractional nuclei charges and an equal amount of electrons. More specifically, the fraction *Z* of the pseudohydrogen atoms used to passivate the Ti dangling bonds and O dangling bonds is 4/3 (^{4/3}H) and 2/3 (^{2/3}H),¹⁰ respectively. As in the previous study¹⁰ on the rutile TiO₂ nanodots, the surface Ti atoms have at most two dangling bonds, and the surface O atoms have only one dangling bond. This method provides an ideal passivation to pair the electrons in the dangling bonds and removes the surface states from the energy band gap. In all calculations on wires, we have used a supercell geometry by adding a 10 Å thick layer of vacuum around the wire and repeating the wire+vacuum unit cell periodically.

We have calculated four nanowires of different sizes for the type-I, and three for the other three types. Because of the building method, all of the nanowires are chemical stoichiometrical. The four type-I nanowires are (TiO₂)₅^{4/3}H₆^{2/3}H₆, (TiO₂)₁₃^{4/3}H₁₀^{2/3}H₁₀, (TiO₂)₂₅^{4/3}H₁₄^{2/3}H₁₄, and (TiO₂)₄₁^{4/3}H₁₈^{2/3}H₁₈.

**Figure 2.** Four types of cross sections for nanowires in this study: the blue spheres represent the Ti atoms, the green ones represent the O atoms, and the red and cyan ones represent corresponding pseudohydrogen atoms. In each figure, we plot the projection of the tetragonal primitive lattice as a reference.**TABLE 2: LDA Energy Band Gap, *E_g*, for the Nanowires of Different Size and Different Shape^a**

| | Type-I | Type-II | Type-III | Type-IV |
|---------------------------|--------|---------|----------|---------|
| <i>n</i> | 5 | 13 | 25 | 41 |
| <i>d</i> (Å) | 8.150 | 13.141 | 18.224 | 23.338 |
| <i>E_g</i> (eV) | 1.823 | 1.798 | 1.729 | 1.692 |
| <i>n</i> | 4 | 16 | 32 | |
| <i>d</i> (Å) | 7.289 | 14.579 | 20.618 | |
| <i>E_g</i> (eV) | 2.598 | 2.0182 | 1.853 | |
| <i>n</i> | 9 | 21 | 45 | |
| <i>d</i> (Å) | 10.934 | 16.702 | 24.450 | |
| <i>E_g</i> (eV) | 2.033 | 1.845 | 1.786 | |
| <i>n</i> | 12 | 37 | 76 | |
| <i>d</i> (Å) | 12.626 | 22.170 | 31.774 | |
| <i>E_g</i> (eV) | 2.056 | 1.774 | 1.772 | |

^a *n* is the number of (TiO₂) units in the unit cell of the wire, and *d* is the effective diameter calculated by $\sqrt{2na^2/\pi}$.

**Figure 3.** The band gap, *E_g*, as a function of the diameter *d* of the nanowires in the different structures. The function for the nanodot¹⁰ is also shown for comparison.

The three type-II nanowires are (TiO₂)₄^{4/3}H₄^{2/3}H₄, (TiO₂)₁₆^{4/3}H₈^{2/3}H₈, and (TiO₂)₃₂^{4/3}H₁₂^{2/3}H₁₂. The three type-III nanowires are (TiO₂)₉^{4/3}H₆^{2/3}H₆, (TiO₂)₂₁^{4/3}H₁₀^{2/3}H₁₀, and (TiO₂)₄₅^{4/3}H₁₄^{2/3}H₁₄. Also, the three type-IV nanowires are (TiO₂)₁₂^{4/3}H₈^{2/3}H₈, (TiO₂)₃₇^{4/3}H₁₄^{2/3}H₁₄, and (TiO₂)₇₆^{4/3}H₂₀^{2/3}H₂₀. Their effective diameters are estimated by $\sqrt{2na^2/\pi}$, where *n* is the number of (TiO₂) units in the unit cell of the wire, and *a* is the LDA optimized lattice parameter listed in Table 1.

The calculated LDA band gap for all of the nanowires of different size and different shape are listed in Table 2. For the bulk TiO₂ in the rutile structure, the LDA band gap is 1.68 eV, which is much smaller than the experimental value,¹⁶ 3.0 eV, due to the well-known LDA error. The same error exists in the wire calculations. However, the LDA results are qualitatively credible. A previous study on the Si nanowires¹⁷ shows that the LDA band gap shift can describe the quantum confinement effect very well, via comparing the results of the GW and LDA calculations. The band gap shift is defined as $\Delta E_g = E_g - E_g^{\text{bulk}}$, where *E_g* and *E_g^{bulk}* are the band gap of the TiO₂ nanocrystal and bulk, respectively. Our previous study on the quantum confinement effect in TiO₂ dot with near-spherical shape¹⁰ shows good agreement with the experiments.⁷ Fitting the band gap values with a function $\Delta E_g = \beta_0/d^{\alpha_0}$, we obtain a curve as $\Delta E_g = 73.70/d^{1.93}$ for the nanodot. Here, we also fit the calculated band gap using the function $E_g = E_g^{\text{bulk}} + \beta/d^\alpha$ for the four types of the nanowires. The fitted curves are presented in Figure 3, where the band gap as a function of the nanowire

TABLE 3: α and β for the β/d^α Fitting, and β' for the β'/d^{α_0} Fitting of the E_g for Nanowires in Different Structures^a

| | type-I | type-II | type-III | type-IV |
|------------------|---------|---------|----------|---------|
| α | 1.28 | 1.51 | 1.62 | 2.01 |
| β | 2.25(5) | 18.56 | 17.06 | 60.95 |
| β' | 9.49 | 43.84 | 36.57 | 49.44 |
| β'/β_0 | 0.129 | 0.595 | 0.496 | 0.671 |

^a The ratio of β'/β_0 is also calculated.

effective diameter is plotted. We also fit the band gap of the nanowires using the same function but with α fixed at 1.93, resulting in $E_g = E_g^{\text{bulk}} + \beta'/d^{\alpha_0}$. With the same α , we can compare the quantum confinement effect in the wires and dot via the ratio of β'/β_0 . All of the parameters, α , β , β' , and the ratio of β'/β_0 are shown in Table 3.

From the figure and the fitting parameters, we find that the quantum confinement effect in nanowires becomes significant for $d < 25$ Å. Also, a notable anisotropy of the quantum confinement effect exists. The quantum confinement effect is much weaker in the type-I nanowires, which are surrounded by the (100) crystal planes. While it seems not so important that the center of the nanowire is a Ti atom (type-II) or a Ti–Ti pair (type-III), the difference between type-II and type-III is much smaller than that between type-I nanowires and the other ones. For the type-IV nanowires, the band gap shift is similar to the type-II and type-III ones. That is to say, in the type-IV nanowires, the quantum confinement effect is not limited by the existence of the (100) crystal plane surfaces. The ratio of β'/β_0 for the last three types of nanowires seems close to the simple effective mass results of 0.586, while for the type-I nanowires, the ratio is much smaller, with a value of only 0.129. According to the effective mass model, ΔE_g is inversely proportion to μ , the reduced mass of the effective mass of the electron (m_e^*) and hole (m_h^*). So we calculate the effective masses along the (100) and (110) directions, based on the LDA band structure. The m_e^* and m_h^* along the (100) direction are $1.088m_0$ and $3.485m_0$, respectively, where m_0 is the static mass of electron. Also, the m_e^* and m_h^* along the (110) direction are $0.817m_0$ and $0.331m_0$, respectively. Because of the LDA overbending error, the calculated effective mass is far smaller, but the trend is still qualitatively convincing. Next, we obtain the reduce effective mass along the (100) and (110) direction: $\mu_{100} = 0.829m_0$ and $\mu_{110} = 0.235m_0$. The ratio of μ_{100}/μ_{110} is about 3.5, and the ratio of β' for type-I and type-III (type-II) is 3.8 (4.6). From this comparison, we can conclude that the anisotropy of the quantum confinement effects results from the anisotropy of the effective masses.

The wave function squares of the VBM and CBM states have been calculated for all of the nanowires. In Figure 4, we plot these wave function squares of one selected nanowire for each type. For simplicity, only the views in the cross section planes are shown. First, the wave functions are mostly distributed in the interior of the wire rather than localized on the surface, which indicates the effects of the surface passivation. Second, both the VBM and the CBM states in the nanowires have the same atomic characteristics of the corresponding states in the bulk. The electronic structure of the bulk TiO₂ in the rutile structure has been studied before.^{10,18} For the bulk, the VBM state mainly consists of the O-2p_π orbitals, which are distributed symmetrically at the two sides of the OTi₃ plane, and the CBM state mainly consists of the Ti-3d orbitals with the t_{2g} symmetry. From the patterns in Figure 4, these two characteristics are clearly illustrated. Third, the CBM wave functions are distributed along straight lines in the Ti-centered nanowires, while in the

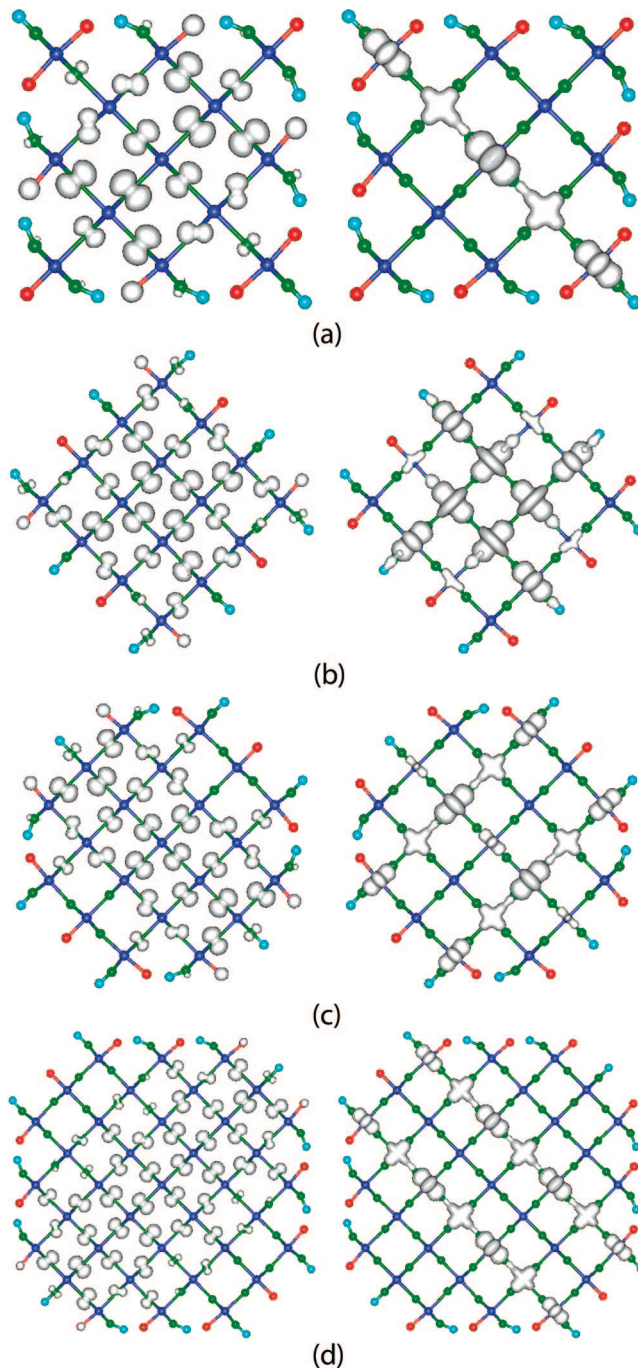


Figure 4. The single-particle wave function squares of the VBM (left) and CBM (right) states for the nanowires (a) (TiO₂)₁₃^{4/3}H₁₀^{2/3}H₁₀, (b) (TiO₂)₁₆^{4/3}H₈^{2/3}H₈, (c) (TiO₂)₂₁^{4/3}H₁₀^{2/3}H₁₀, and (d) (TiO₂)₃₇^{4/3}H₁₄^{2/3}H₁₄, in the structure of type-I, type-II, type-III, and type-IV, respectively.

type-II nanowires a spiral-arms pattern appears. Further investigation shows that the CBM wave functions in all of the nanowires are mainly distributed from the center atoms to the surface oxygen atoms along the shortest paths. We find that the end points of the distribution patterns are TiO₆ clusters [TiO₄^{4/3}H₂ in Figure 4a, TiO₆ in b, and TiO₅^{4/3}H in c and d] with strong contraction. Also, the bond lengths of the Ti–O bonds along the paths are also shorten, except for those directly connecting to the terminal TiO₆ clusters. This strain field is a possible reason for the wave function distributions.

The frequency-dependent dielectric functions $\varepsilon(\omega) = \varepsilon_1(\omega) + i\varepsilon_2(\omega)$ have been evaluated within the electric-dipole approximation. The real part $\varepsilon_1(\omega)$ can be obtained from the

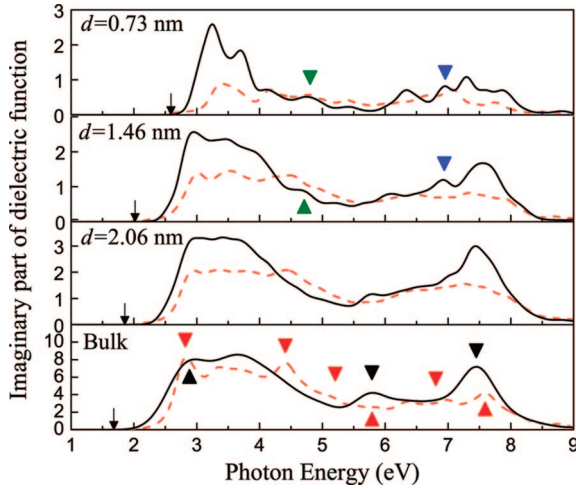


Figure 5. Imaginary part of the dielectric function for the three type-II nanowires and bulk TiO_2 in the rutile structure. The black solid lines are $\epsilon_2^{\parallel}(\omega)$, and the red dashed lines are $\epsilon_2^{\perp}(\omega)$. For the bulk, the positions of the peaks in $\epsilon_2^{\parallel}(\omega)$ and $\epsilon_2^{\perp}(\omega)$, which will be tabulated in Table 4, are indicated using triangles in black and red, respectively.

imaginary part $\epsilon_2(\omega)$ via the Kramers–Kronig relation, while $\epsilon_2(\omega)$ can be calculated as

$$\epsilon_2(\omega) = \frac{4\pi^2 e^2 \hbar}{m^2 \omega^2} \sum_{ij} \frac{2}{(2\pi)^3} \int_{\text{BZ}} dk |M_{ij}(k)|^2 \delta[\omega - \omega_{ij}(k)]$$

where the integral is over all states in the Brillouin zone and the sum is over all combinations between the valence band i and the conduction band j , whose wave functions and energy levels are denoted as $\{\Psi_i, E_i\}$ and $\{\Psi_j, E_j\}$, respectively. Next, the matrix element between band i and j at k is written as $M_{ij}(k) = \langle \Psi_j(k) | \hat{e} \cdot \mathbf{p} | \Psi_i(k) \rangle$, and $\hbar \omega_{ij}(k) = E_j - E_i$. Here, e and p denote the polarization vector and the momentum operator, respectively. We have calculated the frequency-dependent dielectric functions for all of the nanowires, as well as the bulk. For all four different types of nanowires, the trends as the size decreases are similar, so we will only discuss the dielectric functions of the type-II nanowires as a case study in the following.

Figure 5 shows the calculated $\epsilon_2(\omega)$ for three type-II nanowires and bulk TiO_2 in the rutile structure. $\epsilon_2(\omega)$ are evaluated for the polarization along the axial (c) direction [$\epsilon_2^{\parallel}(\omega)$], and for the polarization in the plane perpendicular to the axial direction [$\epsilon_2^{\perp}(\omega)$]. For the bulk TiO_2 in the rutile structure, the locations of the structural features are marked with triangles in Figure 5. In Table 4, we compare these locations to previous experiment¹⁹ and theory work.¹⁸ In the low photon energy region, our results are in good agreement with the previous theory work, if we align the absorption edge (the band gap in ref 18 is 2.0 eV, and our result is 1.68 eV). Because of the LDA error, the fundamental absorption edge is underestimated by about 1.25 eV. However, in the higher photon energy region, our results agree with the experiment well.

For all of the nanowires and the bulk, a direct band gap exists at Γ , but the direct dipole transition is forbidden. As the size of the nanowire decreases, the edge of the absorption is shifted to higher photon energy, and $\epsilon_2(\omega)$ demonstrates a stronger and stronger anisotropy in the two polarization direction, due to the quantum confinement effect. As shown in Figure 5, the absorption edge and main peak in $\epsilon_2^{\parallel}(\omega)$ move toward the LDA band gap (arrows) when d decreases. We attribute this trend to the mixing of the bulk states in the finite-size nanowires, which enhance the dipole transition. We believe that this enhancement

TABLE 4: Structure in the Imaginary Part of the Dielectric Functions for Polarizations Perpendicular ($\epsilon_2^{\perp}(\omega)$) and Parallel ($\epsilon_2^{\parallel}(\omega)$) to the c Axis: Comparison between the Experiment,¹⁹ Previous Theory Work,¹⁸ and This Work^a

| experiment | theory | this work |
|------------|----------------------------------|-----------|
| | $\epsilon_2^{\perp}(\omega)$ | |
| 4.11 | 3.06 | 2.86 |
| 6.63 | 6.15 | 5.77 |
| 7.87 | 7.27 | 7.46 |
| | $\epsilon_2^{\parallel}(\omega)$ | |
| 4.00 | 3.06 | 2.84 |
| 5.35 | 4.67 | 4.42 |
| 6.10 | 6.06 | 5.85 |
| 7.40 | 6.96 | 6.69 |
| 8.05 | 7.59 | 7.58 |

^a The band gap is 3.0, 2.0, and 1.68 eV in the three works, respectively.

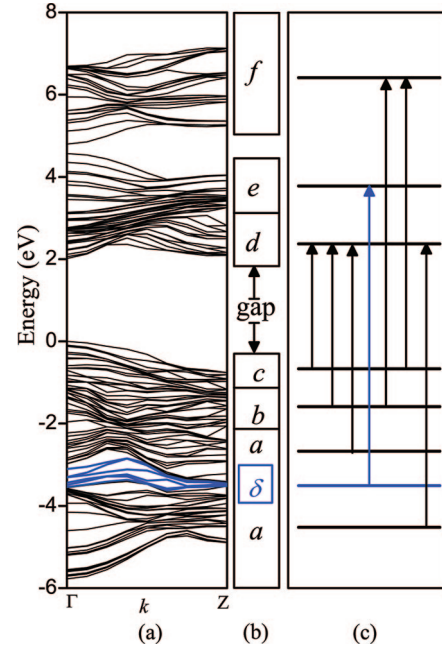


Figure 6. (a) Band structure for the nanowire $(\text{TiO}_2)_{16}/_{4/3}\text{H}_8/_{2/3}\text{H}_8$ in the structure of type-II. The top of the valence band is taken as the zero of energy. (b) Labeling of the energy regions according to the bonding diagram in ref 20 for later reference. (c) Schematic diagram of the optical transitions. The blue bands (in energy region “d”) are the states mainly localized on the surface passivating atoms.

also leads to the appearance of a new peak at about 5.0 eV, which is more notable in the two smaller nanowires, as marked with green triangles in Figure 5.

To discuss the fine structure in $\epsilon_2(\omega)$, we plot the band structure of the $d = 1.46$ nm nanowire in Figure 6a. In this work, we have adopted a wire geometry with a bulk-like structure in the interior, so the Ti-centered distorted octahedron is still the structure unit for the nanowires as in the bulk. Also, we find that the bonding diagram of the TiO_2 perfect crystal (rutile) proposed by Soratin and Schwarz²⁰ is still suitable to analyze the band structure of the nanowires. According to the bonding diagram, the valence band can be decomposed into three parts: the σ bonding of the O p_o and Ti e_g states in the lower energy region; the π bonding of the O p_{π} and Ti e_g in the middle energy region; and the O p_{π} states in the higher energy region. The lower conduction band can be decomposed into two parts: the Ti t_{2g} states interact with each other in the lower energy region; and the π antibonding of the Ti t_{2g} and O p_{π} states in

the higher energy region. The upper conduction band consists of the σ antibonding between the O p_π and Ti e_g states. Our calculations agree with this diagram, and we label the six regions in sequence with “a”, “b”, “c”, “d”, “e”, and “f” in Figure 6b. The bands in the lower part of region “a” are more dispersive because of the contributions from the Ti s orbitals. The blue bands in Figure 6a, corresponding to the energy region labeled by “ δ ” in the diagram, consist of the surface states mainly localized at the surface passivation atoms. The wave function squares of the VBM and CBM states in Figure 4b also confirm the bonding diagram, as discussed above.

In Figure 6c, we plot the schematic diagram of the optical transitions. From the band structure and the amplification of the transition matrix elements $M_{ij}(k)$, we can analyze the fine structure of $\epsilon_2^{\parallel}(\omega)$ for this nanowire: the absorption edge results from the transition between the top bands in region “c” and the bottom bands in region “d”; the broad peak between 3.0 and 4.0 eV results from the transitions between bands in region “c” and region “d”; the peak indicated by the green triangle results from the transitions between the bands in region “b” and region “d”, which is not prominent in the spectrum of the bulk; the peak located at about 6.1 eV, which corresponds to the peak at 5.77 eV in the bulk, results from the transition between the bands in the upper “a” region and the bands at the top of region “d”; the new peak indicated by the blue triangle arises from transitions between the passivating surface states in region “ δ ” and bands in region “e”; and the broad peak between 7.5 and 8.0 eV mainly results from the transition between bands in regions “b”, “c” and “f”, and partly results from the transition between bands in the lower part of region “a” and region “d”.

In conclusion, the quantum confinement effect, electronic properties, and optical properties of TiO₂ nanowires in the rutile structure are investigated via first-principles band-structure calculations. We studied the change of the band gap when the size decreases and fit the results using the function $E_g = E_g^{\text{bulk}} + \beta/d^\alpha$. Four different structures of the nanowires along the c axial direction are considered to investigate the shape-dependence of the quantum confinement effects. We find that the quantum confinement effect in the nanowires surrounded by (100) crystal planes is much weaker than the others. The quantum confinement effect becomes significant for $d < 25$ Å. The imaginary part of the frequency-dependent dielectric function ($\epsilon_2(\omega)$) is evaluated within the electric-dipole approximation, for both the polarization along the axial (c) direction [$\epsilon_2^{\parallel}(\omega)$] and that in the plane perpendicular to the axial

direction [$\epsilon_2^{\perp}(\omega)$]. Because of the quantum confinement effect, the anisotropy in the two polarization direction is stronger as the size decreases. Some new structures in the $\epsilon_2^{\parallel}(\omega)$ appear due to the quantum confinement and the surface passivation. The band structure of the nanowires is calculated, with which the fine structure of $\epsilon_2^{\parallel}(\omega)$ has been analyzed.

Acknowledgment. J.L. gratefully acknowledges financial support from the “One-hundred Talents Plan” of the Chinese Academy of Sciences. We also acknowledge Jürgen Furthmüller for utilizing his code²¹ to calculate the optical properties.

Note Added after ASAP Publication. This article posted ASAP on December 2, 2008. In the second paragraph of this paper, sentences 4 and 5 have been revised. The correct version posted on December 18, 2008.

References and Notes

- (1) Chen, X.; Mao, S. S. *Chem. Rev.* **2007**, *107*, 2891. and references therein.
- (2) O'Regan, B.; Grätzel, M. *Nature* **1991**, *353*, 737.
- (3) Kislyuk, V. V.; Dimitriev, O. P. *J. Nanosci. Nanotechnol.* **2008**, *8*, 131.
- (4) Law, M.; Greene, L. E.; Johnson, J. C.; Saykally, R.; Yang, P. *Nat. Mater.* **2005**, *4*, 455.
- (5) Enache-Pommer, E.; Boercher, J. E.; Aydil, E. S. *Appl. Phys. Lett.* **2007**, *91*, 123116.
- (6) Zhu, K.; Vinzant, T. B.; Neale, N. R.; Frank, A. J. *Nano Lett.* **2007**, *7*, 3739.
- (7) Satoh, N.; Nakashima, T.; Kamaikura, K.; Yamamoto, K. *Nat. Nanotechnol.* **2008**, *3*, 106.
- (8) Monticone, S.; Tufeu, R.; Kanaev, A. V.; Scolan, E.; Sanchez, C. *Appl. Surf. Sci.* **2000**, *162*, 565.
- (9) Kormann, C.; Bahnemann, D. W.; Hoffmann, M. R. *J. Phys. Chem. B* **1988**, *92*, 5196.
- (10) Peng, H.; Li, J.; Li, S.-S.; Xia, J.-B. *J. Phys. Chem. C* **2008**, *112*, 13964.
- (11) Li, J.; Wang, L.-W. *Chem. Mater.* **2004**, *16*, 4012.
- (12) (a) Kresse, G.; Furthmüller, J. *Phys. Rev. B* **1996**, *54*, 11169. (b) Kresse, G.; Furthmüller, J. *Comput. Mater. Sci.* **1996**, *6*, 15.
- (13) Kresse, G.; Joubert, D. *Phys. Rev. B* **1999**, *59*, 1758.
- (14) Monkhorst, H. J.; Pack, J. D. *Phys. Rev. B* **1976**, *13*, 5188.
- (15) Abrahams, S. C.; Bernstein, J. L. *J. Chem. Phys.* **1971**, *55*, 3206.
- (16) Pascual, J.; Camassel, J.; Mathieu, H. *Phys. Rev. Lett.* **1977**, *39*, 1490.
- (17) Zhao, X.; Wei, C. M.; Yang, L.; Chou, M. Y. *Phys. Rev. Lett.* **2004**, *92*, 236805.
- (18) Glassford, K. M.; Chelikowsky, J. R. *Phys. Rev. B* **1992**, *46*, 1284.
- (19) Cardona, M.; Harbeke, G. *Phys. Rev.* **1965**, *137*, A1467.
- (20) Sorrain, P. I.; Schwarz, K. *Inorg. Chem.* **1992**, *31*, 567.
- (21) <http://www.freeware.vasp.de/VASP/optics/>.

JP807439Q